ACS OMEGA

http://pubs.acs.org/journal/acsodf

Article

Characterization and Release Mechanisms of Aerogel-Encapsulated Biocide Crystals for Low-Loading and High-Utilization Antifouling Coatings

Tenna Frydenberg, Claus E. Weinell, Kim Dam-Johansen, Eva Wallström,* and Søren Kiil

Cite This: *ACS Omega* 2022, 7, 34824−34838

Read Online

ACCESS | Metrics & More | Article Recommendations | Supporting Information

ABSTRACT: Silica aerogel-encapsulated biocide crystals can potentially enhance the protection efficiency of antifouling coatings, thereby lowering the impact on nontarget aquatic life. In the present study, copper pyrithione (CuPT) crystals are encapsulated by silica aerogel to obtain loadings of 50−80 wt % CuPT. For optimal design of the heterogeneous particles and mapping of the underlying biocide release mechanisms, the aerogel-encapsulated biocide crystals are characterized by scanning (transmission) electron microscopy, energy-dispersive X-ray spectroscopy, thermal gravimetric analysis, mercury intrusion porosity, Brunauer−Emmett−Teller analysis, and light scattering. The microscopic examination demonstrates that the elongated CuPT crystals are encapsulated by a thin highly porous silica layer. When varying the CuPT loading of the aerogels, it is possible to tune the particle size, pore volume, and specific surface area of the aerogels. Furthermore, this study suggests that the hydrophilic aerogel-encapsulated CuPT, when used in antifouling coatings, attracts seawater and contributes to an efficient controlled release of active CuPT.

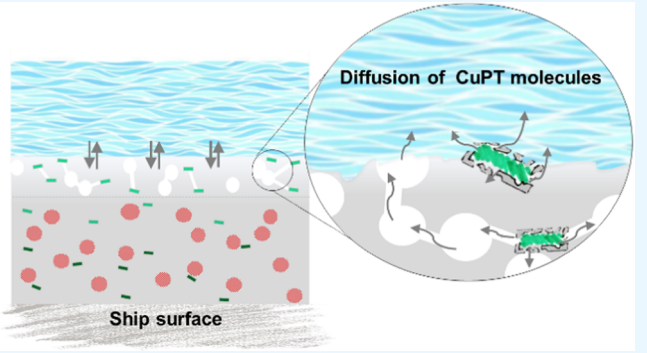

1. INTRODUCTION

More than 80% of the global trade falls within overseas transport.[1] To prevent the growth of biofouling organisms, such as diatoms, algae, invertebrates, mussels, and barnacles, as well as the associated drag increase, fouling control coatings are applied extensively on underwater vessel surfaces.[2] By 2025, the annual global fouling control market is projected to reach 193.000 tons, with shipping vessels, fishing boats, and yachts accounting for around 80% of the market share.[1,3]

The term "fouling control" covers the two main technologies: conventional antifouling coatings, containing active biocides, and fouling release coatings (both with and without biocides) with a low surface energy and high flexibility, which, upon movement of the vessel, "washes off" the biofouling. When working efficiently, fouling control coatings, relative to fouled ship hulls, ensure a reduced fuel consumption and lower emissions of CO_2, NO_x, and SO_2, as well as a more limited spread of invasive species. Currently, the coating market is dominated (>90%) by antifouling coatings, which very slowly release biocides into the surrounding seawater.[3]

To obtain a broad-spectrum impact on biofouling species, cuprous oxide (Cu_2O) is typically used in a combination with one or more approved organic booster biocides, such as zinc ethylene bisdithiocarbamate (Zineb), 4,5-dichloro-2-octyl-2*H*-isothiazol-3-one (DCOIT), tralopyril, copper pyrithione (CuPT), zinc pyrithione (ZnPT), dichlofluanid, tolylfluanid, and/or medetomidine.[4] However, a major problem is the nonoptimal release rate control of the organic biocides. To obtain sufficient surface protection, a high biocide loading of the coating is required. This is because the small biocide molecules diffuse rapidly through the pigment-leached (i.e., porous) coating matrix into the surrounding water environment without necessarily exploiting the full potential of the individual molecules.[5−7] In addition, due to the polishing rate of the coating surface, poorly water-soluble biocide particles, such as copper pyrithione (CuPT),[8] may be released from the coating surface as solid particles, as opposed to dissolved molecules. When this occurs, the biocide is not fully exploited for the intended purpose, and an excessive dose is needed to reach the required antifouling protection. Consequently, the oceans are advertently polluted, which increases the risk of antimicrobial resistance.[9]

Encapsulation of the biocide is an efficient way to optimize the release rate, and this approach is frequently used across industries, e.g., pharmacology,[10] food,[11] medicine,[12] cosmet-

Received: May 20, 2022
Accepted: September 7, 2022
Published: September 22, 2022

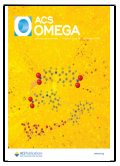

ics,[13] and agriculture.[14−16] Reasons for doing so include compound degradation protection, modification of the physical material characteristics, controlled or targeted release rates, mixing of incompatible compounds, and stability improvements. For anticorrosive coatings, where corrosion inhibitors are encapsulated in microcapsules and released by external stimuli, such as a pH change, the concept has been thoroughly investigated.[17,18]

In the case of biocides for antifouling coatings, oil-in-water (O/W) emulsions and polymeric microcapsules, in particular, have been explored for encapsulation purposes,[19−27] as detailed in Table 1. Microcapsules are generally used to protect UV-sensitive biocides like 3-iodo-2-propynyl butylcarbamate (IPBC) and/or prevent premature release of easily degradable biocides. Furthermore, microcapsules can facilitate the coating formulation and impede an undesired plasticization of the coating films.[28−30] The release from nonporous microcapsules is typically realized by the rupture and prompt liberation of the biocide, resulting in a potential undesired peak-like delivery. Additionally, when using microcapsules, Reybuck et al. emphasized the need for biocides for the initial control of microorganisms by also having free biocides in the coating.[29] Mesoporous capsules, utilized for controlled release via a pore structure, are commonly loaded with biocides through physical adsorption, where the capsules are presoaked in a biocidal solution.[31] However, an inherent disadvantage of this pore-filling method is the fast and easy leakage of liquid biocides from the pore structure.[32]

The antifouling performance and the biocide release rate are significantly influenced by the coating matrix (i.e., binder and pigments).[44] Nevertheless, only a limited number of the studies in Table 1 have considered coating testing in natural seawater or a quantitative evaluation of the biocide release rate. When using physical encapsulation, the biocide is not chemically modified and therefore does not fall in the category of a new biocidal product. Consequently, the required risk assessments and approvements, which are costly and time-consuming, can be avoided.[45] A promising strategy toward more environmentally friendly and sustainable coatings with prolonged antifouling protection periods is the use of a physical encapsulation of a commercially available biocide.

In this paper, the synthesis and characterization of CuPT crystals encapsulated by silica aerogels are presented. The aim was to find the maximum CuPT loading capacity of the aerogels and to investigate how their properties change with the loading. In this regard, the understanding of the aerogel encapsulation properties is important for designing loaded aerogels and a controlled biocide release and to be able to quantify the biocide release mechanism for an antifouling coating. To formulate an antifouling coating with functionalities for a given application, it is necessary to know the type and amount of encapsulating material needed to obtain acceptable physical properties and achieve the required antifouling protection. Important formulation parameters, such as the ratio between pigment volume concentration and critical pigment volume concentration (PVC/CPVC, also named λ), are a function of the particle size distribution (PSD), the particle shape, the surface morphology, and the particle-binder physicochemical affinity.[46] Additionally, to achieve optimal physical properties, antifouling protection, and maximum service life, it is essential to know the optimal ratio between encapsulated CuPT and the silica matrix.

2. OVERALL MECHANISMS OF THE AEROGEL−BIOCIDE APPROACH

In 2009, Wallström et al. demonstrated the first attempts toward an encapsulation technology with the potential of achieving higher biocidal efficiency of commercial organic biocides (i.e., zinc and copper pyrithione), thereby reducing the overall biocide demand in an antifouling coating for yachts.[40,47] According to the patent WO2011107521,[47] one or more biocidal compounds, during a sol−gel process followed by supercritical CO_2 drying, are entrapped in silica aerogels. The latter, together with pigments, are subsequently dispersed in the coating formulation, and the original expectation was that the aerogel slowly wears at the coating−seawater interface and contributes to the polishing of the coating. Upon this action, the biocides were expected to release and effectively protect the surface against biofouling.[40,47] Proof-of-concept studies (unpublished[48]) demonstrated the effectiveness of the encapsulation approach, as shown in Figure 1, for antifouling coating performance after 1 year of exposure (June 2018−2019).

The static panel exposure test was performed at two locations (Horsens and Jyllinge) in the presence of both soft (e.g., slime and algae) and hard (e.g., barnacles) fouling species. For reference, a commercial yacht antifouling coating and a noncoated blank were used. Compared to these references, the experimental aerogel-based coating with 3.7 wt % biocide (CuPT), despite a few barnacles attached to the coated area exposed in Horsens, showed promising biofouling resistance in the Danish harbors. For shipping vessels, the coating needs to perform in multiple and extreme fouling environments, and the inclusion of Cu_2O is generally required. Furthermore, shipping vessels require an extended protection period of the coating for 5−7 years.

To understand the function of silica aerogels, it is highly relevant to explore the workings of a polishing antifouling coating. Figure 2 illustrates the mechanisms of a traditional polishing antifouling coating containing nonencapsulated biocides.

In traditional coatings, the release of biocides (soluble pigments and organic compounds), after a few weeks of seawater exposure, leaves behind a micrometer-thick leached layer. Due to chemical reactions and seawater friction, the thickness of the leached layer, in well-functioning coatings, remains constant (under constant seawater conditions). This reduces the diffusion resistance of the dissolved biocides and ensures an adequate and continuous leaching of biocides.[49]

When using aerogel encapsulation of the poorly soluble CuPT crystals, the time available for the biocide particles to dissolve, due to aerogel-induced water absorption in the outer coating layers, is expected to increase. This, in turn, prevents premature displacement loss from the coating surface of nondissolved crystals and ensures an optimal use of the biocide. Inside the aerogel skeleton, dissolving CuPT crystals form a saturated solution from, which the biocide is released and subsequently diffuses through the porous matrix toward the coating surface.

In summary, the aerogel encapsulation, with a strong adhesion between the biocide and the aerogel, is expected to have the following technological advantages: (I) high porosity and water-induced hydrophilic properties, which enhance the local dissolution rate of the biocide. (II) Maintaining, due to diffusion-controlled biocide release through the pores of the

https://doi.org/10.1021/acsomega.2c03133
ACS Omega 2022, 7, 34824−34838

Table 1. Recent Studies on Encapsulation of Active Compounds for Coating Applications[a]

publication year	active compound	encapsulant	encapsulation method	coating system	performance testing	application	references
2020	DCOIT	porous silica nanoparticles	sol−gel synthesis	antibacterial/antifouling polymer coating	field test of coated panels, antifouling assay, nontarget toxicity test	marine coatings	Michailidis et al.[33]
2020	irgarol	calcium alginate hydrogels	microfluid emulsion-based external gelation	NA	release studies from hydrogels in suspension; antifouling effect tested using water grass	wood protection	Liu et al.[34]
2020	DCOIT	silica submicrocontainers	O/W emulsion	NA	NA	marine coatings	Aidarova et al.[28]
2020	capsaicin, silicon oil	PUF microcapsules	O/W emulsion polymerization	zinc acrylate resin	real-sea tests of coatings	marine coatings	Li et al.[35]
2020	econea	polymeric capsules	spray-drying	water-based acrylic and polyurethane binder	field test of coated fishing nets	fishing nets	Kartal et al.[36]
2020	ZS, UA	silica nanosystem	O/W miniemulsion	NA	antifouling in vitro tests	outdoor surface protection	Ruggiero et al.[27]
2019	DCOIT	polyurea capsules	surface polycondensation	NA	NA	marine coatings	Aidarova et al.[19]
2019	MBT	silica nanosystem (capsules and particles)	polymerization	NA	release studies in aqueous solution	outdoor surface protection	Ruggiero et al.[37]
2018	ZS	silica nanocapsules	O/W emulsion	NA	release studies in aqueous solution	marine coatings	Ruggiero et al.[20]
2018	capsaicin	chitosan nanocapsules	microemulsion	NA	pH-responsive antibacterial property of nanocapsules	marine coatings	Wang et al.[38]
2017	DCOIT	polymeric microcapsule	O/W emulsion	water-based coatings	field test of coated fishing nets; release studies from coating simulated in a flow cell	fishing nets	Callenti et al.[21]
2017	irgarol, econea, and ZnPT	PLA nanoparticles	O/W emulsion	commercial water-based antifouling coating	release studies from nanoparticles in suspension	wood protection	Kamtsikakis et al.[22]
2017	CuPT, ZnPT	silica nanocapsules	O/W emulsion	NA	toxicity testing—growth inhibition tests	marine coatings	Avelelas et al.[23]
2015	DCOIT, MBT	silica nanocapsules	O/W emulsion	PU (water-based) and epoxy (solvent-based) coatings	microbiological studies of nanocapsules in suspension and coatings; release studies from suspension	marine coatings	Maia et al.[24]
2013	sodium benzoate	polymeric microcapsules	polymerization	NA	growth inhibition tests and release studies	wood protection	Jämsä et al.[39]
2011	ZnPT	silica aerogels (SA)	sol−gel synthesis	rosin/acrylic binder	field test of coated panels; release studies from gels in suspension	marine coatings	Wallström et al.[40]
2011	silver compound	polymeric microspheres	O/W emulsion	unknown coating	field test of coated glass; release from microspheres in suspension	marine coatings	Szabó et al.[25]
2011	IPBC	PMMA	O/W emulsion	NA	NA	outdoor surface protection	Nordstierna et al.[26]
2010	medetomidine	PMMA microspheres	emulsification−solvent evaporation	exterior wall coatings (water- and solvent-based)	release studies from microspheres in coatings	outdoor surface protection	Nordstierna et al.[7]
2010	IPBC	silica microparticles	emulsion	water-based commercial coating	release studies from coatings. UV stability test. In vitro release studies	wood protection	Sørensen et al.[41]
2009	DCOIT	PVA microcapsules and phenolic resin	emulsification and cross-linking	biocide-free waterborne coating	NA	underwater protection	Hart et al.[30]
2008	chlorhexidine	PLA	emulsification−solvent evaporation	NA	testing antibacterial activity	marine coatings	Fäy et al.[42]
2007	DCOIT	amino-formaldehyde capsules	emulsion	unknown coating	Leaching from polymer films	marine coatings	Reybuck et al.[29]
2007	DCOIT	PMMA−BA nanocapsules	two-stage miniemulsion	PMMA-based coating	release from coated glass	marine coatings	Zhang et al.[43]

https://doi.org/10.1021/acsomega.2c03133
ACS Omega 2022, 7, 34824−34838

Table 1. continued

[a]O/W = oil in water. NA = not available. DCOIT, 4,5-dichloro-2-octyl-2*H*-isothiazol-3-one; ZS, zosteric acid sodium salt; UA, usnic acid; MBT, 2-mercaptobenzothiazole; econea, tralopyril, 4-bromo-2-(4-chlorophenyl)-5-(trifluoromethyl)-1*H*-pyrrole-3-carbonitrile; PUF, poly(urea-formaldehyde); ZnPT, zinc pyrithione; IPBC, 3-iodo-2-propynyl butylcarbamate; PLA poly(L-lactide); PMMA–BA, poly(methyl methacrylate-*co*-butyl acrylate); and PVA, poly(vinyl alcohol).

aerogel, an adequate rate of biocide release over a prolonged period of time.

3. EXPERIMENTAL SECTION

3.1. Materials for the Preparation of Aerogels. Methyl ester of orthosilicic acid (tetramethyl orthosilicate, Dynasylan M) was used as a precursor and purchased from Evonik Industries (Essen, North Rhine-Westphalia, Germany). Copper pyrithione (CuPT, Copper Omadine) was acquired from Lonza Group AG (Basel, Switzerland). A mixture of absolute ethanol (EtOH, 99.8%) and deionized water was used as a solvent and an aqueous ammonia solution (NH_3, 25%) as the catalyst to accelerate the hydrolysis and condensation process.

3.2. Preparation of Silica Aerogels with Copper Pyrithione. As illustrated in Figure 3, silica aerogels and encapsulation of CuPT biocide were prepared by a sol–gel process followed by supercritical CO_2 drying according to Wallström et al.[40]

The silica aerogel samples were prepared by a two-step sol–gel method: a precursor solution of tetramethoxysilane (TMOS), ethanol, and water was prepared with selected molar ratios and mixed under stirring. For CuPT-loaded aerogels, a CuPT powder was added to the precursor solution. To catalyze the hydrolysis and condensation processes, an aqueous ammonia solution was subsequently added. For each sample, gelation occurred at room temperature within 45 min after the addition of the aqueous ammonia solution. After complete gelation, the wet gel was stored in ethanol for mechanical enhancement of the silica network. Following aging, the wet silica gels were cut into smaller pieces, using a knife, and dried for 4 h under supercritical CO_2 conditions (110 bar and 40 °C). Using 2 mm glass beads and a mechanical shaker for 15 min, all granular samples were ground to powders. The characterization study included four different synthesized silica aerogels with CuPT loadings from 50 to 80% by weight (Table 2). As a reference sample, pure silica aerogel (SA) was produced under the same synthesis conditions as the loaded ones.

3.3. Silica Aerogel Characterization. The morphology of the silica aerogels obtained was characterized by scanning (transmission) electron microscopy (SEM/STEM) coupled with energy-dispersive X-ray spectroscopy (EDS) (Prisma E, Thermo Fisher Scientific). Analyses were conducted at 15 keV. To avoid charging effects, the SEM samples were sputtered with a 5 nm thin layer of silver, while STEM samples were prepared by dispersing aerogel powder in ethanol and drop-casting onto a grid. Particle size and shape were quantified using the software ImageJ. Particle size distributions were obtained from a quantitative two-dimensional (2D) evaluation of three SEM images with 20–40 particles in each micrograph. Thermal stability and biocide content were estimated by thermogravimetric analysis (TGA, Mettler M 3, Toledo). The measurements were carried out under a nitrogen blanket with a heating rate of 10 °C/min in the temperature range of 50–800 °C. To quantify particle size distributions, using a nonspherical form factor and a refractive index input of n = 1.4585, light scattering (Mastersizer 3000, Malvern) in an ethanol medium was applied. All samples were sonicated (Bandelin Sonorex, Buch & Holm) for 5 min before measurement. A size range interval was applied to the particle size distributions (after measurement) for obtaining the volume-weighted mean diameter $D[4,3]$ of individual peaks, given as

https://doi.org/10.1021/acsomega.2c03133
ACS Omega 2022, 7, 34824–34838

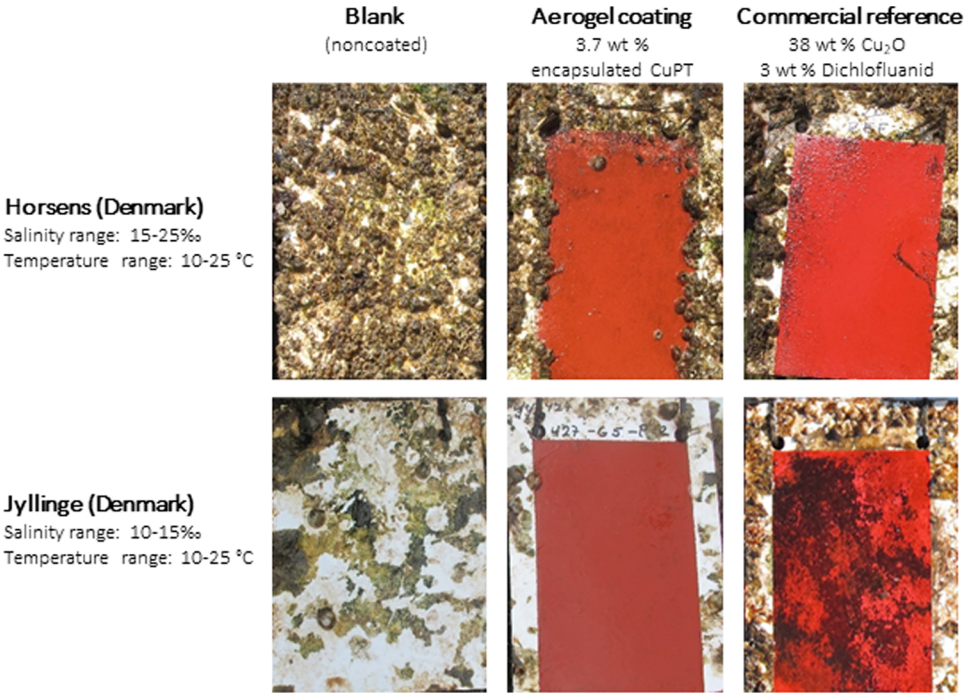

Figure 1. Static antifouling performance of experimental coatings based on the aerogel encapsulation technology. Coatings were exposed for 12 months in two Danish harbors (55°51′27.7″N 9°52′36.9″E and 55°44′41.9″N 12°05′41.4″E). Left column: blank (noncoated) panel of acrylic. Middle column: experimental coating containing 3.7 wt % aerogel-encapsulated CuPT (no other biocides in the formulation). Right column: commercial reference containing 38 wt % Cu_2O and 3 wt % dichlofluanid (concentrations provided on a solvent-inclusive basis).

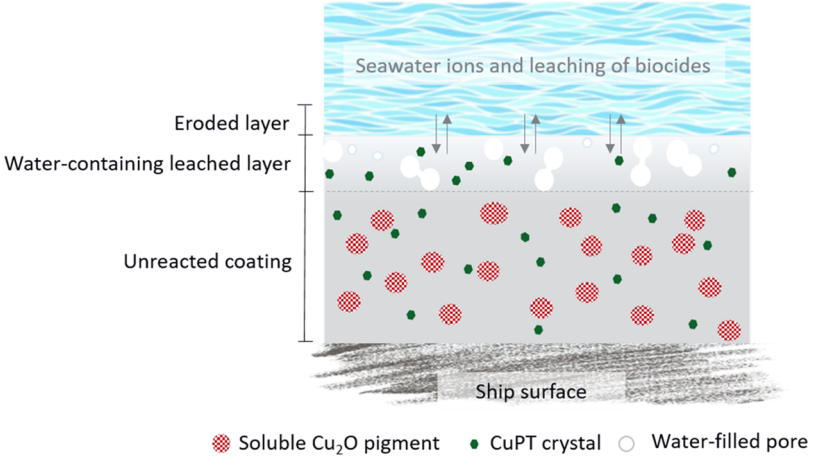

Figure 2. Schematic illustration of the working mechanisms of a traditional polishing antifouling coating containing nonencapsulated CuPT crystals. Due to their low seawater solubility, partially dissolved CuPT crystals are present in the leached layer. Most organic biocide particles do not have sufficiently long seawater contact to fully dissolve and are consequently lost as crystals at the coating−seawater interface. Note that the sketch is not to scale.

$$D[4,3] = \frac{\sum n_i \cdot D_i^4}{\sum n_i \cdot D_i^3}$$

where n_i is the (number-based) frequency of occurrence of particles in size class i, having a mean diameter D_i.

The textural properties were evaluated based on the adsorption isotherms at liquid nitrogen temperature (77 K), performed on a NOVAtouch LX^2 equipment (Quantachrome Instruments), and with the samples degassed at 150 °C for 8 h. Using the Brunauer−Emmett−Teller (BET) method, the specific surface area (S_{BET}) was estimated. Pore volume, bulk density, apparent density, total porosity, and median pore diameter were determined by mercury intrusion porosimetry (MIP) (AutoPore V, Micromeritics). Bulk densities were measured at 100 kPa, while apparent densities were obtained by increasing the pressure to 200 MPa. An apparent density included a space between particles and pores down to 6.6 nm in diameter. The method is based on the Washburn model, assuming cylindrical-shaped pores with open ends, closed pores, and that narrow-opening pores are not included. The median pore diameter is calculated based on the low- to high-pressure pore size distribution. Uncertainties of pore volume (0.49 ± 0.02 mL/g) and diameter (6.8 ± 0.5 nm) were obtained from a measurement on a standard material. Oil absorption (OA) values of aerogels were estimated according to the standard method ISO 787-5:1980.[50]

https://doi.org/10.1021/acsomega.2c03133
ACS Omega 2022, 7, 34824−34838

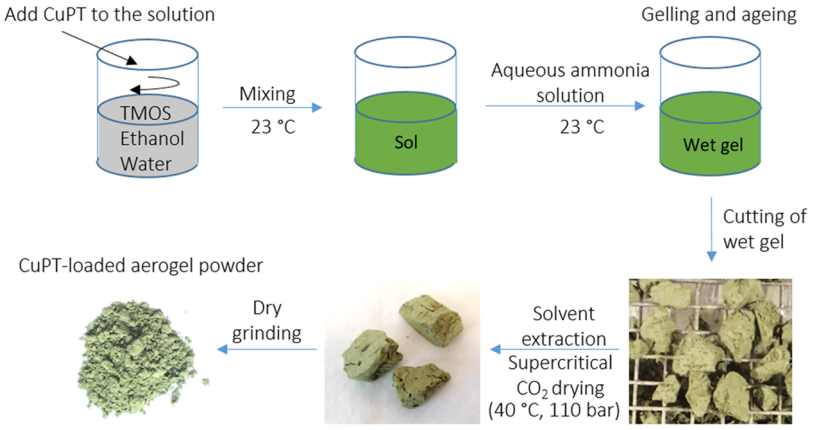

Figure 3. Procedure for the preparation of CuPT-loaded silica aerogels.

Table 2. CuPT Loading and Gelation Time of Silica Aerogels[a]

	CuPT loading		gelation time
sample name	(wt %)	(vol %)	(min)
SA	0	0	15
C50SA	50	5	25
C65SA	65	10	45
C75SA	75	15	17
C80SA	80	20	35

[a]The gelation time is a visual measure of the point in time at which the viscosity of the solution increases steeply (seen as gelation).

To separate aerogel particles with respect to size, a sedimentation experiment with centrifugation and subsequent measurement of the particle size distribution by light scattering was performed. For the analysis, a 250 mg aerogel powder was dispersed in 10 mL ethanol (15 mL tube) and centrifuged for 1 min at 500 rpm followed by 5 min at 1500 rpm. Due to the different sedimentation rates, two distinct phases appeared. The upper supernatant phase was removed, while the bottom phase, to remove the remaining silica residuals, was washed several times by centrifugation and redispersed in ethanol. Finally, the sample was dried in a desiccator at room temperature. Prior to the light scattering measurement, the dried sample was redispersed in ethanol and sonicated for 1 min.

The hydrophilic groups of the aerogels were identified using a Fourier transform infrared (FTIR) spectrometer (Thermo Scientific Nicolet iS5), equipped with an iD7 attenuated total reflectance (ATR) diamond crystal. An average FTIR spectrum from eight scans with a resolution of 4 cm^{-1} and performed in the range of 500−4000 cm^{-1} was collected.

A simple swelling test was performed by sticking a fine granulate powder of CuPT-loaded aerogels onto a Petri disc using a 3M double-sided adhesive tape. Powder not firmly attached to the surface was removed by compressed air. Optical imaging, using a VHX-6000 digital microscope from KEYENCE, was subsequently performed before and during exposure to demineralized water at different time intervals. Any occurring swelling was observed and recorded as an increase in the individual granulate size. To provoke maximum swelling, demineralized water, as supposed to artificial seawater, was used.

4. RESULTS AND DISCUSSION

In the following sections, an in-depth characterization of silica aerogels with various CuPT loadings is presented and discussed. Based on the characterization study, the primary working principles of aerogel-encapsulated CuPT crystals in an antifouling coating are elucidated.

4.1. Properties of Silica Aerogels. *4.1.1. Morphology, Size Distribution, and Elemental Analysis.* The morphology and size distribution of pure CuPT crystals and synthesized aerogels (with and without loading) were investigated by scanning electron microscopy (SEM). The results are presented in Figure 4.

Pure elongated CuPT crystals are seen in Figure 4a, and the corresponding particle size distribution is shown in Figure 4b with a narrow distribution centered around 2.1 ± 1 μm. Synthesized pure silica aerogels (SA), on the other hand, presented in Figure 4c,d, have an irregular morphology and a broad size distribution with a mean dimension of 11 ± 4.4 μm. However, as shown in Figure 4e, aerogels resulting from the encapsulation of CuPT crystals have two distinct morphologies: the small particles were mostly elongated, very similar to pure CuPT crystals, while the larger particles or clusters exhibited an irregular shape. This suggests that the morphology of the biocides has a major impact on the properties of the silica aerogels. In addition, the original crystal shape of CuPT was almost unaffected by the conditions of the aerogel synthesis. Under gelling conditions, due to poor solubility in distilled water and ethanol (used in the precursor solution and in the supercritical drying fluid), CuPT crystals are expected to be stable. However, the aerogel shape is most likely affected by the dispersion of CuPT in the precursor polymer solution. Figure 4f shows the two particle size distributions of the elongated (blue histogram) and irregular-shaped particles (orange histogram), both obtained from sample C75SA. The mean length of elongated particles was 2.2 ± 0.9 μm, slightly larger than the pure CuPT crystals, while the irregular particles have a broad size distribution centered around 8.5 ± 3.8 μm.

Generally, the morphology of the aerogel influences the orientation and packing structure in a coating film, and the efficiency of packing is a function of the shape, size, and size distribution of the particles. Due to the enhanced packing ability of the smaller aerogels, which fill the voids between the larger ones or pigments, the broad particle size distribution of the aerogels increases the maximum packing fraction. In addition, relatively large-aspect-ratio particles, like the

https://doi.org/10.1021/acsomega.2c03133
ACS Omega 2022, 7, 34824−34838

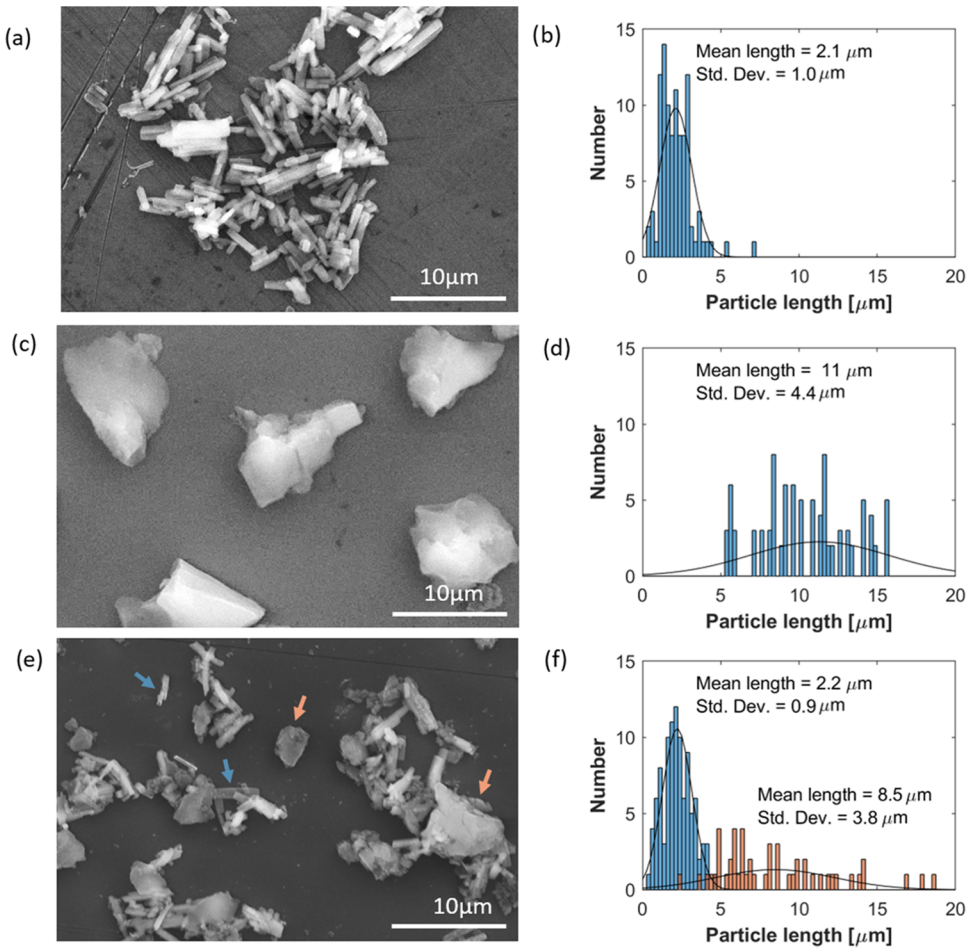

Figure 4. SEM images and the corresponding size distributions of (a, b) pure CuPT crystals, (c, d) pure silica aerogels (SA), and (e, f) CuPT crystals encapsulated by silica aerogels (sample C75SA). The distributions were obtained from manual analysis of SEM images in ImageJ software, and the term "length" refers to the greatest dimension of the particles. Arrows, in colors corresponding to their size distribution, indicate two distinct morphologies of sample C75SA.

elongated aerogels, have the potential to pack in a dense manner with a longitudinal orientation, while disorientation of aerogels will result in a loose packing structure. This, in turn, can affect the water penetration of the coating and, thereby, the release rate of the biocide.

To illustrate the range of particle shapes and validate the encapsulation, high-magnification high-angle annular dark-field scanning transmission electron microscopy (HAADF-STEM) images of the aerogel sample C75SA (Figure 5a–d) were obtained. Elemental analysis of the particles seen in Figure 5a, where silicon, oxygen, carbon, nitrogen, copper, and sulfur were detected, revealed the presence of both silica and CuPT in the elongated particles (Figure S1). This confirms that the small elongated particles consist of a core–shell-like structure in which the CuPT crystal core is coated by a porous silica layer. Additionally, elemental analysis of the large two-piece particle shown in Figure 5d confirmed that both the upper and lower parts consisted of silica and CuPT. In addition to the EDS point scan analysis, Figure 5e shows an EDS line scan analysis across a single rectangular silica-coated CuPT crystal. Here, the Si signal (pink) clearly proves the presence of a silica layer at the surface of the crystal.

A centrifugation (sedimentation) operation with sample C75SA in an ethanol solution, followed by a particle size distribution measurement (Figure S2), confirmed, even though a smaller fraction of cluster particles, containing CuPT, were also detected in the centrifugation liquid, that it was possible to separate large empty (low density) silica particles. Improving the dispersion of CuPT crystals during gelation by decreasing the number of cluster particles evenly distributes the amount of available silica between the particles. This increases the possibility of the clusters breaking down during grinding. The pure silica residues cannot be avoided; these are a result of the production process.

4.1.2. Estimation of the Loading Capacity of Silica Aerogels. To assess the thermal stability of synthesized silica aerogels and to quantify the amount of CuPT encapsulated, a thermogravimetric analysis (TGA) was performed. The curves for samples SA, C50SA, C65SA, C75SA, C80SA, and pure CuPT, specified in Table 2, are shown in Figure 6.

The weight loss until 250 °C can be attributed to the evaporation of the tightly bound solvent remaining in the pores of the aerogels and to water adsorbed on the surface, while the second weight loss, occurring at a temperature range of 250–550 °C, is the decomposition of CuPT. This weight loss was 34.1, 45.4, 47.8, and 55.0% for samples C50SA, C65SA, C75SA, and C80SA, respectively. As seen in Figure 6b, these values correspond to the expected theoretical losses that can be calculated based on the measured weight loss of SA and CuPT in the same temperature range. Apart from sample C80SA, this

https://doi.org/10.1021/acsomega.2c03133
ACS Omega 2022, 7, 34824–34838

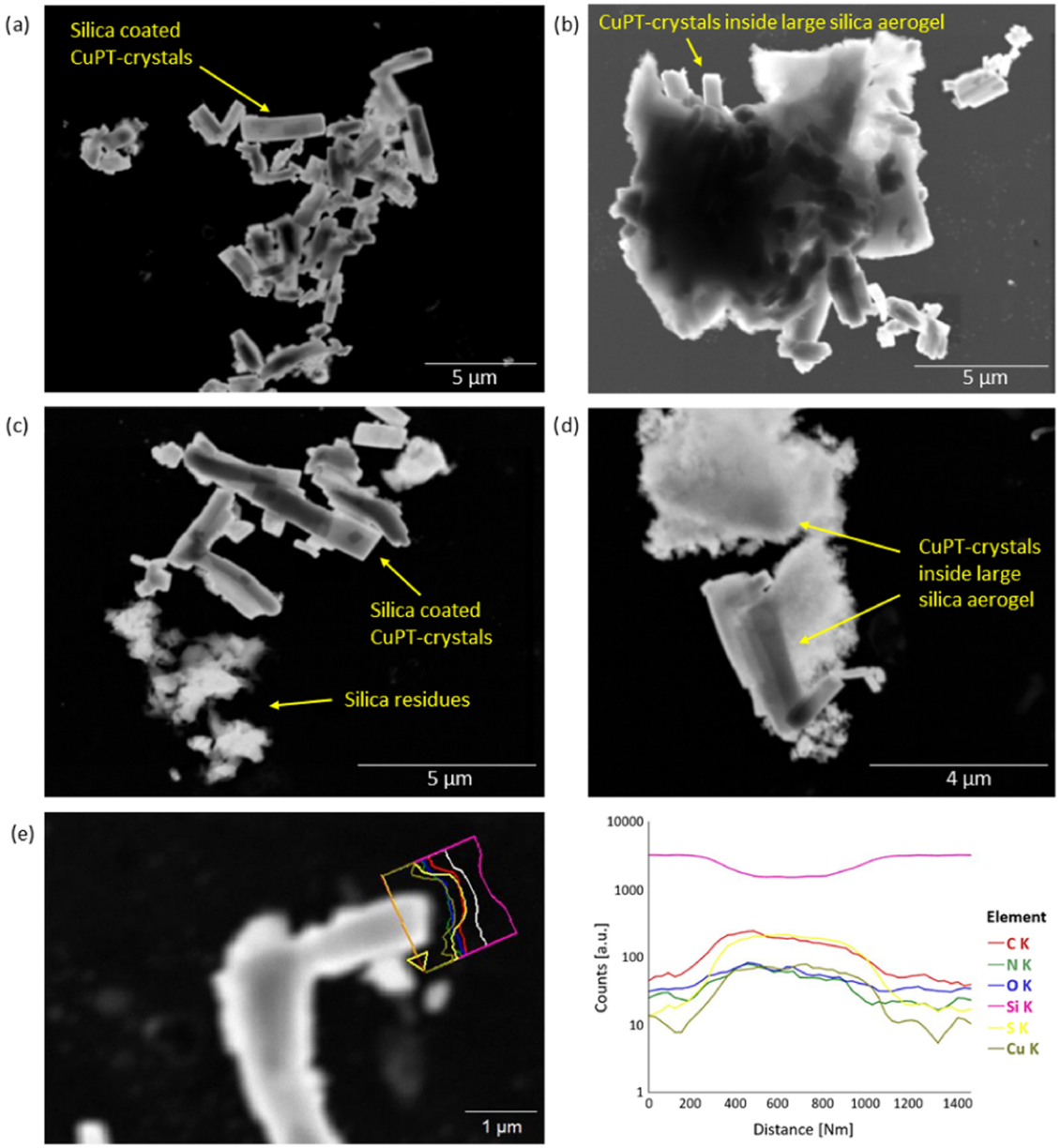

Figure 5. HAADF-STEM images of sample C75SA, illustrating the range of particle shapes. (a) Small elongated CuPT crystals individually coated by porous silica. (b) Elongated CuPT crystals protruded from a large irregular cluster. (c) Silica-coated CuPT crystals and small silica residues. (d) Elongated CuPT crystals inside larger silica aerogel structures. (e) EDS line scan analysis of a single rectangular particle. The yellow arrow on the STEM image indicates the position of the scanned line.

confirms that the percentage matches the intended loading. The weight loss of sample C80SA indicates a loading closer to 90 than 80 wt %, and the additional reduction of weight in region III is ascribed to the final decomposition of CuPT into CuS. In conclusion, the CuPT loading level of the aerogels can be targeted with very high precision, and during the supercritical drying process, there is no biocide loss. A loading level of 80−90 wt % may seem high, but on a volume basis, it only corresponds to 20−35% of the aerogel. Therefore, it is expected that the filling level can be further increased but it poses high requirements on the strength of the aerogel skeleton and it is uncertain that the aerogel properties in the coating will be maintained. Finally, the thermogravimetric curves also confirm because the decomposition profiles are similar to that of CuPT that there are no chemical bonds between the CuPT crystals and the encapsulating silica material. This means that no regulatory biocide approval for the new heterogeneous compound is needed before market implementation.

4.2. Characterization of Copper Pyrithione-Loaded Silica Aerogels. To investigate the influence of CuPT loading, particle size distributions (PSDs) of aerogel samples were measured in suspension by light scattering. Figure 7a shows the PSD of CuPT and SA with a $D[4,3]$ mean diameter of SA on 14.2 ± 0.7 μm. As previously interpreted by Scott for large-aspect-ratio particles,[51,52] the PSD of well-dispersed CuPT crystals is dominated by the peak associated with the "rod diameter", whereas the tail peak at 2.0 μm reflects the length of the elongated crystals, e.g., the "rod length". As expected, the length of CuPT crystals measured using SEM (Figure 4b) and light scattering is similar. The $D[4,3]$ value of CuPT was 0.541 ± 0.002 μm when determined in the size

https://doi.org/10.1021/acsomega.2c03133
ACS Omega 2022, 7, 34824−34838

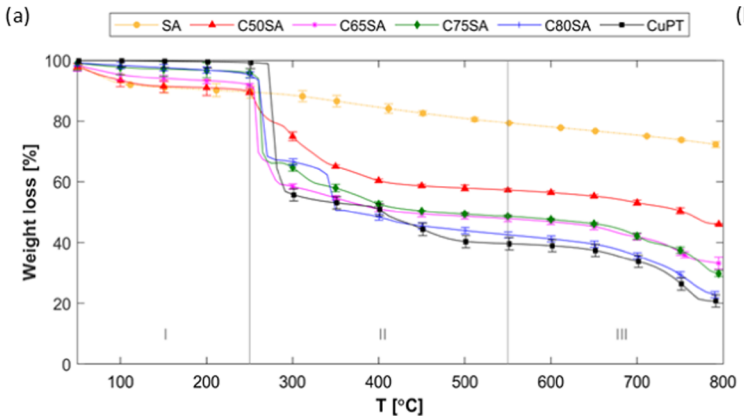

(b) Weight loss [%] b/w 250-550 °C:

	measured	theoretical
SA	12.0±1.1	
CuPT	60.5±0.1	
C50SA	34.1±0.1	36.3±0.6
C65SA	45.4±0.2	43.5±0.4
C75SA	47.8±0.2	48.4±0.3
C80SA	55.0±0.3	50.8±0.2

Figure 6. (a) Thermogravimetric analysis of silica aerogel samples with increasing CuPT loading. The decompositions were divided into three regions, and the weight losses in region II were calculated between temperatures 250 and 550 °C. (b) Summary of weight loss from TGA measurements and theoretical weight loss calculated based on the expected CuPT loading percentage and the measured weight loss of SA and CuPT.

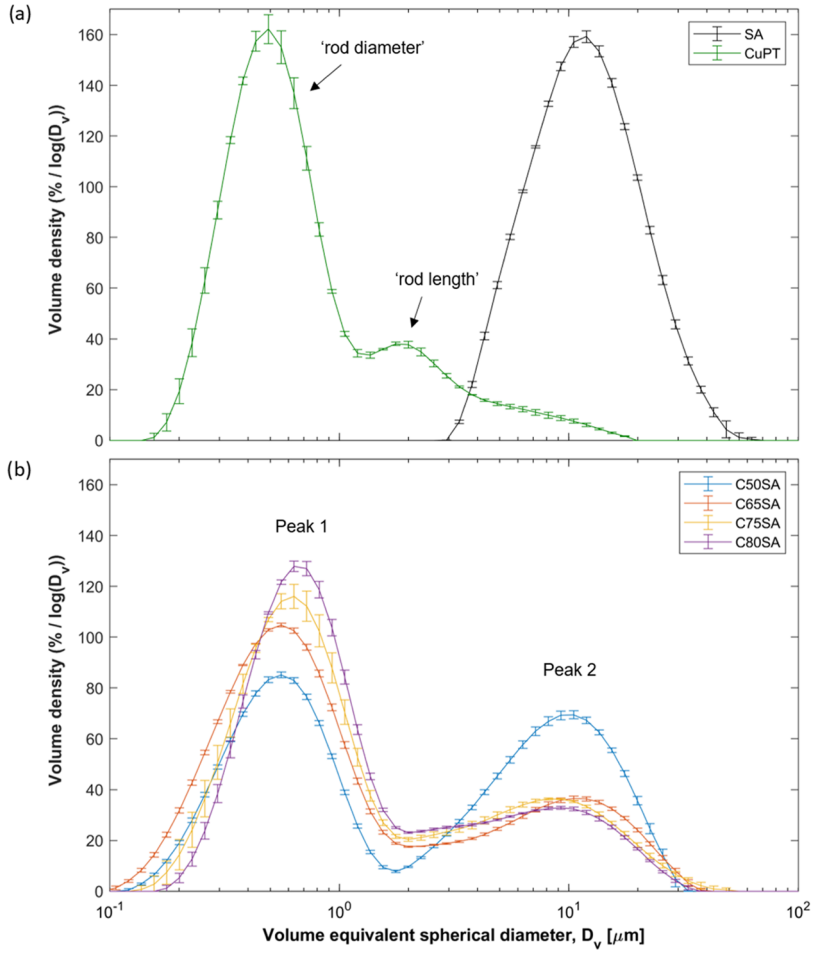

Figure 7. PSDs of (a) sample SA and CuPT and (b) loaded aerogel samples C50SA, C65SA, C75SA, and C80SA. Data obtained by light scattering. Note the log scale on the *x*-axis.

interval of 0−1.2 μm, corresponding to the mean rod diameter. However, a tendency of overestimating the shortest dimension of the particles, e.g., the rod diameter, and underestimating their longest dimension, e.g., the rod length, is present as described by Tinke et al. for rectangular particle systems.[53]

As seen in Figure 7b, the loaded aerogel samples C50SA, C65SA, C75SA, and C80SA show bimodal PSDs. In accordance with the SEM analysis, the first peak of the bimodal PSDs represents coated CuPT crystals, while the second peak represents aerogel clusters and larger pure silica residues. The peak area ratios, given in Table 3, show that larger clusters and silica residues dominate the volume distribution. However, as the CuPT loading increases, a smaller part of the aerogels are assigned to the second peak,

https://doi.org/10.1021/acsomega.2c03133
ACS Omega 2022, 7, 34824−34838

Table 3. Data Obtained from Particle Size Distributions[a]

sample name	$D[4,3]$ (μm) peak 1	$D[4,3]$ (μm) peak 2	peak area ratio $\frac{\text{peak 1}}{\text{peak 2}}$	silica layer thickness[d] (nm)
CuPT	0.541 ± 0.002[b]			
SA		14.20 ± 0.70		
C50SA	0.606 ± 0.018[c]	9.58 ± 0.11	0.06	33 ± 18
C65SA	0.610 ± 0.002[c]	9.39 ± 0.20	0.13	35 ± 3
C75SA	0.711 ± 0.007[c]	9.24 ± 0.71	0.16	85 ± 7
C80SA	0.715 ± 0.009[c]	8.60 ± 0.06	0.19	106 ± 9

[a]Volume-weighed mean diameters ($D[4,3]$) were determined for peak 1 and peak 2. Peak area ratios were calculated as the area between peak 1 and peak 2. Silica layer thickness was estimated from $D[4,3]$ values. [b]CuPT rod diameter, D_{CuPT}. [c]Aerogel rod diameter, $D_{aerogel}$. [d]Silica layer thickness given by $(D_{aerogel} - D_{CuPT})/2$.

implying a reduced amount of silica residues or clusters. Additionally, the mean sizes of silica residue and clusters shift to lower values for higher loading. In comparison, the mean sizes of coated CuPT crystals, corresponding to rod diameter, shift to slightly higher values for increased loading. The mean sizes range from 0.606 ± 0.018 to 0.715 ± 0.009 μm, all slightly larger than that of pure CuPT crystals (Table 3). This indicates a thin silica aerogel layer around the individual CuPT crystals. When assuming a rod shape of the elongated particles and a homogeneous layer of surrounding silica, the silica layer thickness can be estimated based on the differences in mean sizes of particles and pure CuPT crystals (Table 3). The thickness of the silica layer increases with higher CuPT loading; this is attributed to the rheological change during gelation. In an antifouling coating, a thicker layer of porous silica promotes the local aquatic environment around CuPT crystals, thereby increasing the time for dissolution of the low water-soluble biocide.

To understand and adjust the biocide release kinetics, the textural properties, because of their key role regarding biocide diffusion and physical interaction between the biocide and the coating matrix, are important parameters to consider. The textural properties of the aerogel samples have been evaluated by oil absorption (OA), mercury intrusion porosimetry (MIP), and nitrogen adsorption measurements and are summarized in Table 4. To calculate the critical pigment volume concentration (CPVC) for the coating formulations, the OA value is needed and expresses maximum concentration for wettability, which depends on the surface area and morphology of the aerogel. Table 4 shows the decrease in OA value for increased loading of aerogels, which is directly correlated to the decrease in specific surface area (S_{BET}) measured by nitrogen adsorption. The surface area and pore diameter of the CuPT-loaded aerogels are important factors for water absorption and release of biocide and, therefore, also related to antifouling properties. For higher CuPT-loaded aerogels, the median pore diameter obtained by MIP was found to increase, which corresponds to the increased surface area. When the wet gels are formed by gelation under stirring, the pore structure of the resulting silica aerogels depends on the viscosity of the precursor solution. Increasing the CuPT content increases the precursor solution viscosity and the rheological behavior of the wet gel leading to increased pore size.

The total porosity (Φ) was calculated from the following expression

$$\Phi = 1 - \frac{\rho_{bulk}}{\rho_{apparent}} \quad (1)$$

where the ρ_{bulk} and $\rho_{apparent}$ are the bulk and apparent densities obtained by mercury intrusion porosimetry measured at low pressure (100 kPa) and high pressure (200 MPa), respectively. The bulk density includes interparticle voids, while the apparent density includes intraparticle pores up to 6.6 nm. SA aerogels showed the highest total porosity, 72.9%, whereas the total porosity of the loaded aerogels ranged from 64.9 to 68.7%. For sample C75SA, the lowest value was obtained, which can be explained by the short gelation time (Table 2). The faster gelation of the silica skeleton of sample C75SA leads to an increase in the cross-linking degree and a subsequent lower porosity. Furthermore, it can be validated that the water absorption capacity of the aerogels, which originate from their high porosity, is not significantly reduced by the loading of CuPT.

Previous studies indicated that the coating binder penetrates the pores of the aerogel,[47] which increases the adherence of CuPT crystals to the coating matrix and limits the loss of nondissolved CuPT crystals in the outer coating layer. Aerogels with a high specific surface area are expected to increase the penetration of binder, thereby giving a stronger adhesion. Conversely, larger pores also contribute to the penetration of the binder.

4.3. Hydrophilic Groups and Swelling of Copper Pyrithione-Loaded Silica Aerogels. Based on the characterization study, which demonstrated the porous nature of the CuPT-loaded aerogels, the following two mechanisms may be prevalent in an antifouling coating, containing the particles, and exposed to seawater:

(I) Hydrophilic CuPT-loaded silica aerogels attract seawater into their pores.

Table 4. Textural Properties of CuPT-Loaded Silica Aerogels[a]

sample	OA	pore volume (mL/g)	bulk density (g/cm^3)	apparent density (g/cm^3)	total porosity (%)	median pore diameter (nm)	S_{BET} (m^2/g)
CuPT	35.1 ± 0.9	1.34	0.689	1.69	59.2	421	
SA	202 ± 1.9	4.79	0.217	0.80	72.9	14.4	821 ± 44
C50SA	105 ± 2.3	3.45	0.275	0.85	67.6	13.3	208 ± 23
C65SA	99.3 ± 0.8	3.09	0.387	1.24	68.7	20.3	138 ± 10
C75SA	93.6 ± 0.8	2.25	0.475	1.35	64.9	22.1	109 ± 16
C80SA	88.4 ± 0.4	2.30	0.501	1.50	66.6	27.3	80.0 ± 9

[a]Oil absorption (OA) values were estimated according to ISO 787-5:1980. Pore volume, total porosity, median pore diameter, and bulk densities were determined by mercury intrusion measurements. The specific surface area (S_{BET}) was estimated by nitrogen absorption, and the standard deviation reflects three replicates.

https://doi.org/10.1021/acsomega.2c03133
ACS Omega 2022, 7, 34824−34838

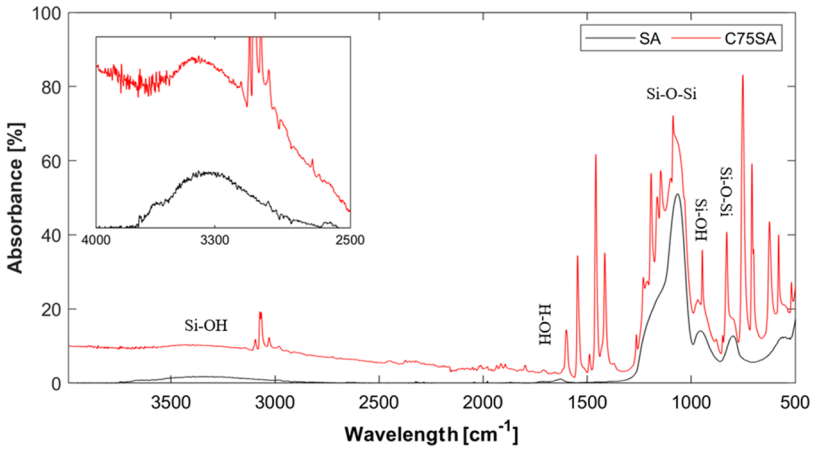

Figure 8. FTIR-ATR spectra of samples SA and C75SA. Vibration modes assigned to the silica aerogel are indicated. Inset: zoomed-in spectra of the overlapping peak of the O−H stretching and SiO−H stretching.

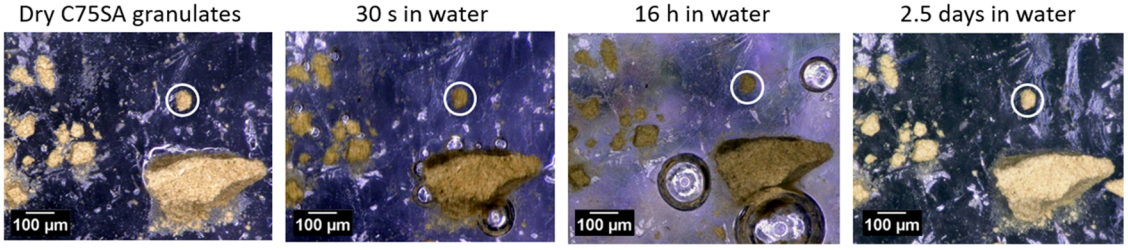

Figure 9. Microscopic images of sample C75SA (fine granulates) in demineralized water after 0−2.5 days of immersion. For transient size comparison, a granulate was encircled.

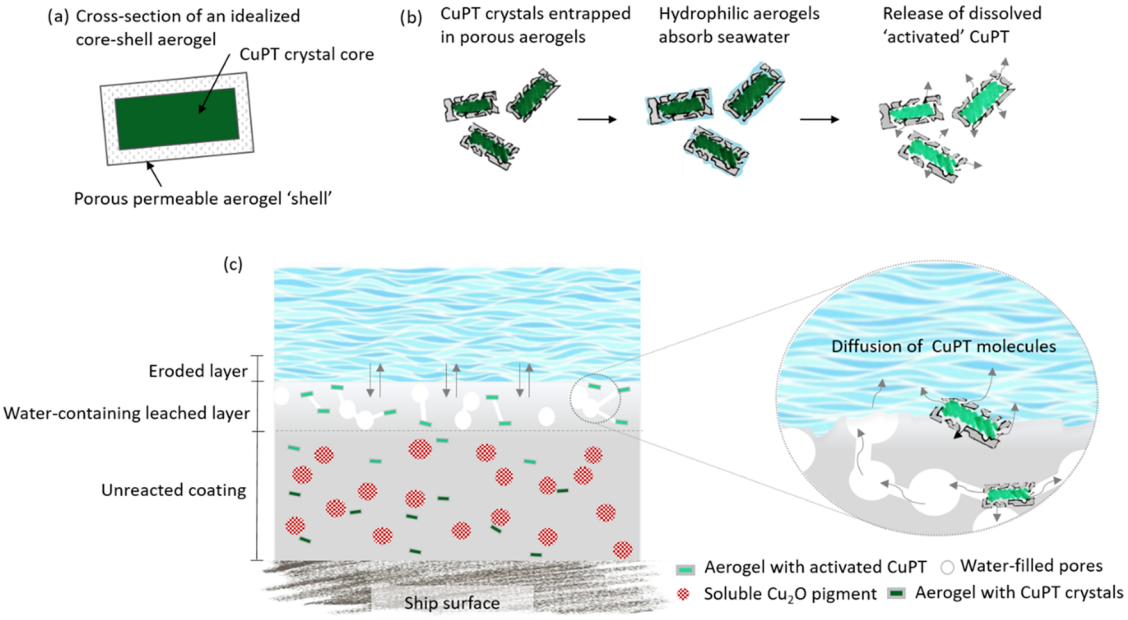

Figure 10. (a) Schematic representation of a CuPT crystal encapsulated in silica aerogel matrix (not to scale). The aerogel encloses the CuPT crystal within a mesoporous silica shell, which allows the penetration of seawater while entrapping the solid CuPT crystal. (b) The working principle of the aerogel material in the coating matrix. (c) A cross-sectional view of an antifouling coating, containing CuPT-loaded aerogels, exposed to seawater. After dissolution of the soluble pigments, a porous leached layer forms. Only activated biocides can diffuse through the leached layer pores and give biocidal protection at the coating surface. Empty aerogels, present in the outermost surface layer, are polished away by the flow of seawater.

(II) CuPT-loaded silica aerogels swell upon seawater exposure.

TMOS-based silica aerogels are inherently hydrophilic,[54] whereas CuPT crystals are hydrophobic. The CuPT-loaded silica aerogels, exhibiting both porous and hydrophilic properties, are expected to be strong absorbents. From FTIR-ATR spectra (Figure 8), where samples SA and C75SA showed common bands assigned to various vibrations

https://doi.org/10.1021/acsomega.2c03133
ACS Omega 2022, 7, 34824−34838

in the silica network, the hydrophilic nature of the encapsulated biocide was confirmed. The broad absorption peak at 3400 cm^{-1} is assigned to the overlapping of the O−H stretching and SiO−H stretching (the latter being the cause of hydrophilic properties), and the peak at 1630 cm^{-1} corresponds to adsorbed water molecules. The peak at 960 cm^{-1} is characteristic of the Si−OH stretching. Due to the presence of surface silanol groups, and hence the hydrophilic nature of these aerogels, water molecules adsorb on the surface of the aerogels. The peaks at 1070, 800, and 560 cm^{-1} originate from the Si−O−Si vibrations of the silica backbone. In addition, the characteristic bond stretching of C−H, C═C, N−O, and C−S at 3026−3095, 1546, 1212, and 709 cm^{-1}, respectively, appeared in the C75SA spectra originating from CuPT crystals. Also, an N−O bending appeared at 832 cm^{-1}.

To investigate whether seawater exposure results in swelling and expansion of the CuPT-loaded aerogels, a simple swelling experiment was conducted. Figure 9 shows dry and wet C75SA aerogel granules.

At the microscale, no visible changes in size were observed for the CuPT-loaded aerogels after seawater exposure, suggesting that the CuPT-loaded aerogels did not swell. Furthermore, no particle collapse was observed, so the aerogels most likely retain their open porous structure in seawater. However, displaced air bubbles visually rose to the water surface, which confirms that the CuPT-loaded aerogels absorb water. Consequently, mechanism I seems the most likely.

4.4. Working Principle of Aerogels in the Coating Matrix. For identification and understanding of the CuPT-loaded aerogels' working mechanisms in an antifouling coating, the characterization of aerogel-encapsulated CuPT crystals is essential. In addition, the characteristics of the aerogels can facilitate the formulation of coatings with aerogel-encapsulated CuPT for various purposes e.g., different aquatic environments, sailing speed, and protection period. Furthermore, to improve biocide release mechanisms, the physical properties of the aerogel can be adjusted.

It was shown above that the highly porous silica aerogels form a "shell" around the CuPT crystals, which helps to control the biocide release rate. Figure 10a shows a schematic representation. The CuPT crystals are effectively trapped inside a thin and porous silica structure, as illustrated in Figure 10b. Due to their hydrophilic nature, aerogels attract seawater upon exposure that enters and fills the pore network. This, over time, secures a local aquatic environment inside the aerogels and a saturated solution of CuPT from dissolving particles. With a rate depending on solubility, hydrophobicity, diffusivity, and degradation of the aerogel structure in the coating−water interface, dissolved CuPT will be released. The hydrophilic properties of the aerogel enhance the time for dissolution of the poorly seawater-soluble CuPT crystals, allowing the maximum possible biocidal function at the coating surface. Additionally, the spatial confinement of the solid CuPT crystals ensures that only dissolved CuPT molecules can diffuse into the pores of the aerogel skeleton. Figure 10c illustrates the new understanding of the mechanisms in an antifouling coating containing aerogel-encapsulated CuPT crystals. As shown, encapsulated CuPT crystals and soluble pigments (e.g., Cu_2O) are distributed throughout the binder matrix. When the coating is exposed to seawater, the binder matrix and soluble pigments begin to react with seawater ions, which creates a porous leached layer.

Marson et al.[55] suggested a mechanism for the establishment of contact between two neighboring pores, from dissolving Cu_2O particles, in the binder: when a particle has been dissolved by seawater to uncover the thin binder film separating it from an as yet unleached particle (deeper down), the solvent (water) will diffuse through the thin membrane and dissolve some of the pigment particles. The resulting osmotic pressure subsequently ruptures the membrane and pores get interconnected. In this way, the release of biocides is driven. Aerogels embedded in the outer coating layer will undergo the mechanisms described in Figure 10b, and CuPT crystals are subsequently dissolved (i.e., activated) and released in the leached layer. Potentially, CuPT-loaded aerogels can replace Cu_2O as a pore-forming agent, with a similar osmotic pressure mechanism driven by CuPT. Due to the large surface area and porous structure, the aerogel, because the binder penetrates the porous structure during preparation, will have a strong adherence to the binder matrix. This likely limits the loss of solid CuPT crystals in the outer surface layer of the coating. In conclusion, the primary function of the aerogels is the establishment of a local aquatic environment and unique adhesion between CuPT crystals and the binder matrix. The diffusion of dissolved CuPT will take place through the pores of fully aerogel-coated CuPT crystals. Therefore, the thickness of the encapsulating layer is of higher significance than the size and connectivity of the pore network. Further studies must be conducted to show the effect of the presence of the aerogels on the polishing rate, which may be associated with the brittleness and/or strength of the aerogel skeleton. Note also that the biocide release mechanism will depend on the environmental conditions (e.g., seawater temperature, pH, dissolved organic matter, salinity, salt constitution, and water flow) prevailing.[56,57]

5. CONCLUSIONS

Silica aerogel-coated CuPT crystals, containing up to 80 wt % CuPT, were successfully obtained through a sol−gel method. To understand the working mechanisms in a coating, an investigation of the morphology, size, and physical properties of the CuPT-loaded aerogels was performed. The results show that the CuPT crystals dictate the appearance of the resulting encapsulated particles. The aerogels consist of micron-sized elongated CuPT crystals, surrounded by a thin porous silica layer, as well as larger silica clusters containing multiple CuPT crystals. Characterization studies showed that the hydrophilic aerogels attract seawater and form a local aquatic environment that extends the time for dissolution of the poorly seawater-soluble CuPT crystals. Spatial confinement of the CuPT crystals and a strong adherence to the coating matrix allow the aerogel to maintain a controlled release of dissolved CuPT over a sustained period. In addition, the total porosity and thickness of the encapsulating layer are influenced by the CuPT loading of the aerogels. All of these factors affect the biocide release rate and provide a fundamental understanding of the working mechanisms.

■ ASSOCIATED CONTENT

Supporting Information

The Supporting Information is available free of charge at https://pubs.acs.org/doi/10.1021/acsomega.2c03133.

EDS point analysis of elongated particles in sample C75SA (Figure S1); illustration of sedimentation

https://doi.org/10.1021/acsomega.2c03133
ACS Omega 2022, 7, 34824−34838

experiment and corresponding particle size distribution (Figure S2); and illustration showing the definition of rod diameters observed in particle size distributions (Figure S3) (PDF)

AUTHOR INFORMATION

Corresponding Author

Eva Wallström − *EnCoat ApS, 2100 København Ø, Denmark;* orcid.org/0000-0003-1652-3925; Email: ewa@encoat.dk

Authors

Tenna Frydenberg − *The Hempel Foundation Coatings Science and Technology Centre (CoaST), Department of Chemical and Biochemical Engineering, Technical University of Denmark (DTU), 2800 Kgs. Lyngby, Denmark; EnCoat ApS, 2100 København Ø, Denmark;* orcid.org/0000-0001-9602-0169

Claus E. Weinell − *The Hempel Foundation Coatings Science and Technology Centre (CoaST), Department of Chemical and Biochemical Engineering, Technical University of Denmark (DTU), 2800 Kgs. Lyngby, Denmark*

Kim Dam-Johansen − *The Hempel Foundation Coatings Science and Technology Centre (CoaST), Department of Chemical and Biochemical Engineering, Technical University of Denmark (DTU), 2800 Kgs. Lyngby, Denmark*

Søren Kiil − *The Hempel Foundation Coatings Science and Technology Centre (CoaST), Department of Chemical and Biochemical Engineering, Technical University of Denmark (DTU), 2800 Kgs. Lyngby, Denmark*

Complete contact information is available at: https://pubs.acs.org/10.1021/acsomega.2c03133

Notes

The authors declare no competing financial interest.

ACKNOWLEDGMENTS

The authors would like to acknowledge the Innovation Fund Denmark for financial support to the project (Grant number 8053-00249B) and the Hempel Foundation for funding CoaST (The Hempel Foundation Coatings Science and Technology Centre). Additionally, the mercury intrusion measurements performed at the Department for Nano Production and Micro Analysis at Danish Technological Institute are acknowledged.

NOMENCLATURE

λ, reduced PVC value (PVC/CPVC)
Φ, total porosity
BET, Brunauer−Emmett−Teller
CPVC, critical pigment volume concentration
CuPT, copper pyrithione
DCOIT, 4,5-dichloro-2-octyl-2H-isothiazol-3-one
D_v, volume equivalent spherical diameter
EDS, energy-dispersive X-ray spectroscopy
HAADF, high-angle annular dark-field imaging
IPBC, 3-iodo-2-propynyl butylcarbamate
MBT, 2-mercaptobenzothiazole
MIP, mercury intrusion porosimetry
NA, not available
OA, oil absorption
O/W, oil in water
PLA, poly(L-lactide)
PMMA-BA, poly(methyl methacrylate-*co*-butyl acrylate)
PVA, poly(vinyl alcohol)
PVC, pigment volume concentration
PSD, particle size distribution
PUF, poly(urea-formaldehyde)
SA, silica aerogel
S_{BET}, specific surface area
SEM, scanning electron microscopy
STEM, scanning transmission electron microscopy
TMOS, tetramethoxysilane
UA, usnic acid
Zineb, zinc ethylene bisdithiocarbamate
ZnPT, zinc pyrithione
ZS, zosteric acid sodium salt

REFERENCES

(1) Asariotis, W. J. R.; Assaf, M.; Ayala, G.; Ayoub, A.; Benamara, H.; Chantrel, D.; Hoffmann, J.; Larouche-Maltais, A.; Premti, A.; Rodríguez, L.; Sun, S.; Youssef, F.; Abbas, H.; Bradford, G.; Cariou, P.; Crowe, T.; Davidson, N.; Manuel, J.; Orejas, D.; Dominioni, G.; Ducrest, J.; Faghfouri, M.; Haag, F.; Ingebrigtsen, M.; Kontou, E.; Lane, A.; Lind, M.; Alcover, A. M.; Milne, J.; Mooney, T.; Notteboom, T.; Pallis, A. A.; Sánchez, R.; Stevenson, A.; Stratidakis, S.; Teodoro, A.; Verhoeven, P. *Review of Maritime Transport*; UNCTAD, 2020.

(2) Callow, M. E.; Callow, J. A. Marine Biofouling: A Sticky Problem. *Biologist* **2002**, *49*, 10−14.

(3) *Global Antifouling Coating Market Research Report—Forecast 2025*; Market Research Future, 2020.

(4) Paz-Villarraga, C. A.; Castro, Í. B.; Fillmann, G. Biocides in Antifouling Paint Formulations Currently Registered for Use. *Environ. Sci. Pollut. Res.* **2022**, *29*, 30090−30101.

(5) Ghosh, S. K.Functional Coatings and Microencapsulation: A General Perspective. *Functional Coatings: By Polymer Microencapsulation*, John Wiley & Sons, Inc., 2006; pp 1−28.

(6) Shtykova, L.; Fant, C.; Handa, P.; Larsson, A.; Berntsson, K.; Blanck, H.; Simonsson, R.; Nydén, M. Ingelsten Härelind, H. Adsorption of Antifouling Booster Biocides on Metal Oxide Nanoparticles: Effect of Different Metal Oxides and Solvents. *Prog. Org. Coat.* **2009**, *64*, 20−26.

(7) Nordstierna, L.; Abdalla, A. A.; Masuda, M.; Skarnemark, G.; Nydén, M. Molecular Release from Painted Surfaces: Free and Encapsulated Biocides. *Prog. Org. Coat.* **2010**, *69*, 45−48.

(8) *Competent Authority Report, Work Programme for Review of Active Substances in Biocidal Products Pursuant to Council Directive 98/8/EC Copper Pyrithione (PT 21)*; Swedish Chemicals Agency (KEMI), 2014.

(9) Khattar, M. M.; Salt, W. G.; Stretton, R. J. The Influence of Pyrithione on the Growth of Micro-organisms. *J. Appl. Bacteriol.* **1988**, *64*, 265−272.

(10) Martínez Rivas, C. J.; Tarhini, M.; Badri, W.; Miladi, K.; Greige-Gerges, H.; Nazari, Q. A.; Galindo Rodríguez, S. A.; Román, R. Á.; Fessi, H.; Elaissari, A. Nanoprecipitation Process: From Encapsulation to Drug Delivery. *Int. J. Pharm.* **2017**, *532*, 66−81.

(11) Brazel, C. S. Microencapsulation: Offering Solutions for the Food Industry. *Cereal Foods Worlds* **1999**, *44*, 388−393.

(12) Ahmed, T. A.; El-Say, K. M. Development of Alginate-Reinforced Chitosan Nanoparticles Utilizing W/O Nanoemulsification/Internal Crosslinking Technique for Transdermal Delivery of Rabeprazole. *Life Sci.* **2014**, *110*, 35−43.

(13) Sakulwech, S.; Lourith, N.; Ruktanonchai, U.; Kanlayavattanakul, M. Preparation and Characterization of Nanoparticles from Quaternized Cyclodextrin-Grafted Chitosan Associated with Hyaluronic Acid for Cosmetics. *Asian J. Pharm. Sci.* **2018**, *13*, 498−504.

https://doi.org/10.1021/acsomega.2c03133
ACS Omega 2022, 7, 34824−34838

(14) Popat, A.; Liu, J.; Hu, Q.; Kennedy, M.; Peters, B.; Lu, G. Q.; Qiao, S. Z. Adsorption and Release of Biocides with Mesoporous Silica Nanoparticles. *Nanoscale* **2012**, *4*, 970−975.
(15) Mattos, B. D.; Tardy, B. L.; Magalhães, W. L. E.; Rojas, O. J. Controlled Release for Crop and Wood Protection: Recent Progress toward Sustainable and Safe Nanostructured Biocidal Systems. *J. Controlled Release* **2017**, *262*, 139−150.
(16) Mishra, M. K. *Applications of Encapsulation and Controlled Release*; CRC Press, 2019; pp 343−400.
(17) Cosmelina, G.; Barbé, C.; Campazzi, E.; Lathière, P. LEIS to Study Corrosion Protection of AA 2024 by Smart Coatings Containing Encapsulated Inhibitors, 2015, pp 0−2.
(18) Maia, F.; Tedim, J.; Lisenkov, A. D.; Salak, A. N.; Zheludkevich, M. L.; Ferreira, M. G. S. Silica Nanocontainers for Active Corrosion Protection. *Nanoscale* **2012**, *4*, 1287−1298.
(19) Aidarova, S. B.; Issayeva, A. B.; Sharipova, A. A.; Ibrashev, K.; Gabdullin, M.; Grigoriev, D. O. Synthesis and Study of the Properties of Containers of DCOIT with the Polyurea Shell. *Int. J. Nanotechnol.* **2019**, *16*, 3−11.
(20) Ruggiero, L.; Crociani, L.; Zendri, E.; el Habra, N.; Guerriero, P. Incorporation of the Zosteric Sodium Salt in Silica Nanocapsules: Synthesis and Characterization of New Fillers for Antifouling Coatings. *Appl. Surf. Sci.* **2018**, *439*, 705−711.
(21) Callenti, F.; Jahic, D.; Mikuz, M.; Vrhun-Ec, A.; Stefanec, D.; Puslar, J. Microencapsulated Biocides, Coating Compositions with Microencapsulated Biocides and Use of Coating Compositions for Fishing Nets. WO2017/095335A, 2017.
(22) Kamtsikakis, A.; Kavetsou, E.; Chronaki, K.; Kiosidou, E.; Pavlatou, E.; Karana, A.; Papaspyrides, C.; Detsi, A.; Karantonis, A.; Vouyiouka, S. Encapsulation of Antifouling Organic Biocides in Poly(Lactic Acid) Nanoparticles. *Bioengineering* **2017**, *4*, No. 81.
(23) Avelelas, F.; Martins, R.; Oliveira, T.; Maia, F.; Malheiro, E.; Soares, A. M. V. M.; Loureiro, S.; Tedim, J. Efficacy and Ecotoxicity of Novel Anti-Fouling Nanomaterials in Target and Non-Target Marine Species. *Mar. Biotechnol.* **2017**, *19*, 164−174.
(24) Maia, F.; Silva, A. P.; Fernandes, S.; Cunha, A.; Almeida, A.; Tedim, J.; Zheludkevich, M. L.; Ferreira, M. G. S. Incorporation of Biocides in Nanocapsules for Protective Coatings Used in Maritime Applications. *Chem. Eng. J.* **2015**, *270*, 150−157.
(25) Szabó, T.; Molnár-Nagy, L.; Bognár, J.; Nyikos, L.; Telegdi, J. Self-Healing Microcapsules and Slow Release Microspheres in Paints. *Prog. Org. Coat.* **2011**, *72*, 52−57.
(26) Nordstierna, L.; Movahedi, A.; Nydén, M. New Route for Microcapsule Synthesis. *J. Dispersion Sci. Technol.* **2011**, *32*, 310−311.
(27) Ruggiero, L.; Bartoli, F.; Fidanza, M. R.; Zurlo, F.; Marconi, E.; Gasperi, T.; Tuti, S.; Crociani, L.; di Bartolomeo, E.; Caneva, G.; Ricci, M. A.; Sodo, A. Encapsulation of Environmentally-Friendly Biocides in Silica Nanosystems for Multifunctional Coatings. *Appl. Surf. Sci.* **2020**, *514*, No. 145908.
(28) Aidarova, S. B.; Issayeva, A. B.; Sharipova, A. A.; Grigoriev, D. O.; Miller, R.; Seilkhanov, T. M.; Babayev, A. A.; Issakhov, M. O. Analysis of NMR Spectra of Submicro-Containers with Biocide DCOIT. *Colloids Interfaces* **2020**, *4*, No. 56.
(29) Reybuck, S. E.; Schwartz, C. Blends of Encapsulated Biocides. US7,377,968B2, 2008.
(30) Hart, R. L.; Virgallito, D. R.; Work, D. E. Microencapsulation of Biocides and Antifouling Agents. US7,550,200B2, 2011.
(31) Chan, A. C.; Cadena, M. B.; Townley, H. E.; Fricker, M. D.; Thompson, I. P. Effective Delivery of Volatile Biocides Employing Mesoporous Silicates for Treating Biofilms. *J. R. Soc., Interface* **2017**, *14*, No. 20160650.
(32) Zheng, Z.; Huang, X.; Schenderlein, M.; Borisova, D.; Cao, R.; Möhwald, H.; Shchukin, D. Self-Healing and Antifouling Multifunctional Coatings Based on PH and Sulfide Ion Sensitive Nanocontainers. *Adv. Funct. Mater.* **2013**, *23*, 3307−3314.
(33) Michailidis, M.; Gutner-Hoch, E.; Wengier, R.; Onderwater, R.; D'Sa, R. A.; Benayahu, Y.; Semenov, A.; Vinokurov, V.; Shchukin, D. G. Highly Effective Functionalized Coatings with Antibacterial and Antifouling Properties. *ACS Sustainable Chem. Eng.* **2020**, *8*, 8928−8937.
(34) Liu, Y.; Nisisako, T. Microfluidic Encapsulation of Hydrophobic Antifouling Biocides in Calcium Alginate Hydrogels for Controllable Release. *ACS Omega* **2020**, *5*, 25695−25703.
(35) Li, Y.; Wang, G.; Guo, Z.; Wang, P.; Wang, A. Preparation of Microcapsules Coating and the Study of Their Bionic Anti-Fouling Performance. *Materials* **2020**, *13*, No. 1669.
(36) Kartal, G. E.; Sarıışık, A. M. Providing Antifouling Properties to Fishing Nets with Encapsulated Econea. *J. Ind. Text.* **2020**, 7569S.
(37) Ruggiero, L.; di Bartolomeo, E.; Gasperi, T.; Luisetto, I.; Talone, A.; Zurlo, F.; Peddis, D.; Ricci, M. A.; Sodo, A. Silica Nanosystems for Active Antifouling Protection: Nanocapsules and Mesoporous Nanoparticles in Controlled Release Applications. *J. Alloys Compd.* **2019**, *798*, 144−148.
(38) Wang, W.; Hao, X.; Chen, S.; Yang, Z.; Wang, C.; Yan, R.; Zhang, X.; Liu, H.; Shao, Q.; Guo, Z. PH-Responsive Capsaicin@chitosan Nanocapsules for Antibiofouling in Marine Applications. *Polymer* **2018**, *158*, 223−230.
(39) Jämsä, S.; Mahlberg, R.; Holopainen, U.; Ropponen, J.; Savolainen, A.; Ritschkoff, A. C. Slow Release of a Biocidal Agent from Polymeric Microcapsules for Preventing Biodeterioration. *Prog. Org. Coat.* **2013**, *76*, 269−276.
(40) Wallström, E.; Jespersen, H. T.; Schaumburg, K. A New Concept for Anti-Fouling Paint for Yachts. *Prog. Org. Coat.* **2011**, *72*, 109−114.
(41) Sørensen, G.; Nielsen, A. L.; Pedersen, M. M.; Poulsen, S.; Nissen, H.; Poulsen, M.; Nygaard, S. D. Controlled Release of Biocide from Silica Microparticles in Wood Paint. *Prog. Org. Coat.* **2010**, *68*, 299−306.
(42) Faÿ, F.; Linossier, I.; Legendre, G.; Vallée-Réhel, K. Micro-Encapsulation and Antifouling Coatings: Development of Poly(Lactic Acid) Microspheres Containing Bioactive Molecules. *Macromol. Symp.* **2008**, *272*, 45−51.
(43) Zhang, M.; Cabane, E.; Claverie, J. Transparent Antifouling Coatings via Nanoencapsulation of a Biocide. *J. Appl. Polym. Sci.* **2007**, *105*, 3826−3833.
(44) Almeida, E.; Diamantino, T. C.; de Sousa, O. Marine Paints: The Particular Case of Antifouling Paints. *Prog. Org. Coat.* **2007**, *59*, 2−20.
(45) Tomoyoshi, C.; Geoff, M. *Biocide Use in Antifouling Coatings: The Regulatory Framework*, National Biofilms Innovation Centre (NBIC-UK), PML Applications Ltd., Singapore Centre for Environmental Life Sciences Engineering (SCELSE) and Singapore National Biofilm Consortium (SNBC), 2020.
(46) Yebra, D. M.; Weinell, C. E. Key Issues in the Formulation of Marine Antifouling Paints. *Advances in Marine Antifouling Coatings and Technologies*, Elsevier Ltd., 2009; pp 308−333.
(47) Jespersen, H. T. Loaded Gel Particles for Anti-Fouling Compositions. WO2011107521, 2011.
(48) Wallström, E.; Andersen, B. H. EnCoat A/S, Internal Company Report: Raft Tests, 2018.
(49) Yebra, D. M.; Kiil, S.; Dam-Johansen, K. Antifouling Technology - Past, Present and Future Steps towards Efficient and Environmentally Friendly Antifouling Coatings. *Prog. Org. Coat.* **2004**, *50*, 75−104.
(50) ISO 787-5:1980. *General Methods of Test for Pigments and Extenders—Part 5 Determination of Oil Absorption Value ISO Standards Handbook: Paints and Varnishes*, 2002; Vol. 3.
(51) Scott, D. M. *Particle Characterization for the Real World TM Interpreting Laser Diffraction Results for Non-Spherical Particles*, Horiba Webinar Series; Advanced Particle Sensors LLC, 2019.
(52) Bohren, C. F.; Huffman, D. R. *Absorption and Scattering of Light by Small Particles*; Wiley: New York, 1998.
(53) Tinke, A. P.; Carnicer, A.; Govoreanu, R.; Scheltjens, G.; Lauwerysen, L.; Mertens, N.; Vanhoutte, K.; Brewster, M. E. Particle Shape and Orientation in Laser Diffraction and Static Image Analysis Size Distribution Analysis of Micrometer Sized Rectangular Particles. *Powder Technol.* **2008**, *186*, 154−167.

https://doi.org/10.1021/acsomega.2c03133
ACS Omega 2022, 7, 34824−34838

(54) Venkateswara Rao, A.; Pajonk, G. M. Effect of Methyltrimethoxysilane as a Co-Precursor on the Optical Properties of Silica Aerogels. *J. Non-Cryst. Solids* **2001**, *285*, 202−209.
(55) Marson, F. Antifouling Paints II. A More Detailed Examination of the Effect of gPigment Volume Concentration. *J. Appl. Chem. Biotechnol.* **1974**, *24*, 515−527.
(56) Ciriminna, R.; Sciortino, M.; Alonzo, G.; de Schrijver, A.; Pagliaro, M. From Molecules to Systems: Sol-Gel Microencapsulation in Silica-Based Materials. *Chem. Rev.* **2011**, *111*, 765−789.
(57) Lavtizar, V.; Kimura, D.; Asaoka, S.; Okamura, H. The Influence of Seawater Properties on Toxicity of Copper Pyrithione and Its Degradation Product to Brine Shrimp Artemia Salina. *Ecotoxicol. Environ. Saf.* **2018**, *147*, 132−138.

https://doi.org/10.1021/acsomega.2c03133
ACS Omega 2022, 7, 34824−34838